Research Article Vol. 9, No. 5 / May 2022 / Optica 485

Terahertz electrometry via infrared spectroscopy of atomic vapor

Shuying Chen,* Dominic J. Reed, Andrew R. MacKellar, Lucy A. Downes, Nourah F. A. Almuhawish, Matthew J. Jamieson, Charles S. Adams, and Kevin J. Weatherill

Department of Physics, Durham University, Durham, DH1 3LE, UK
**Corresponding author: shuying.chen@durham.ac.uk*

Received 22 February 2022; revised 3 April 2022; accepted 3 April 2022; published 29 April 2022

In recent years, the characterization of radiation falling within the so-called "terahertz (THz) gap" has become an ever more prominent issue due to the increasing use of THz systems in applications such as nondestructive testing, security screening, telecommunications, and medical diagnostics. THz detection technologies have advanced rapidly, yet traceable calibration of THz radiation remains challenging. In this paper, we demonstrate a system of electrometry in which a THz signal can be characterized using laser spectroscopy of highly excited (Rydberg) atomic states. We report on proof-of-principle measurements that reveal a minimum detectable THz electric field amplitude of 1.07 ± 0.06 V/m at 1.06 THz (3 ms detection), corresponding to a THz power at the atomic cell of approximately 3.4 nW. Due to the relative simplicity and cryogen-free nature of this system, it has the potential to provide a route to a SI traceable "atomic candle" for THz calibration across the THz frequency range, and provide an alternative to calorimetric methods.

https://doi.org/10.1364/OPTICA.456761

1. INTRODUCTION

The terahertz (THz) frequency range (0.1–10 THz), which lies in the region between electronic/microwave technologies and photonic/infrared technologies, often referred to as the THz gap, has drawn a great deal of interest from a diverse range of disciplines [1]. THz radiation has many desirable features such as its ability to penetrate clothes, cardboard, and other wrappers, while crucially remaining non-ionizing in sensitive biological tissues. This band of radiation has wide-ranging applications [2,3] such as in chemical analysis [4], biomedical science [5], security screening [6], and communications [7]. Great progress has been made over the last three decades in the advancement of THz detection technologies [8], which has enabled these applications.

Techniques for THz detection can be broadly categorized as using thermal, electronic, or photonic detectors [9,10]. Thermal detection methods include bolometers [11–15], Golay cells [16], pyroelectric detectors [17–19], and thermopile detectors [20]. To achieve a low noise floor, high sensitivity, and rapid response times, these detectors require cryogenic temperatures to operate effectively [12,13], leading to high running costs and a large, complex detection apparatus. Electronic detectors are typically based on the photoelectric or photoconductive effect in the detector material. The THz-induced electron movements and other electrical properties in the material are detected to indicate the amplitude of the THz signal [10]. These electronic detectors include photoconductive detectors [21], Schottky junctions [22–25], and field effect transistors (FETs) [26–32] that use various materials, such as carbon nanotubes [26,27], graphene [28], and other semiconductor materials [29–32]. Photonic detectors are sensitive to optical signals that indicate the presence of a THz field. Photomixer systems have been reported for broadband continuous wave (CW) THz detection [33–35]. Nonlinear electro-optical crystals are used to sense THz fields by detecting the polarization change in the laser light transmitted through them as a result of incident THz fields [36–38].

Continued advances in THz technology and applications necessitate robust and accurate characterization of THz radiation. THz intensity or power calibration is typically based on source-based radiometry, such as a calculable blackbody radiation source [39–43], or on a detector-based radiometry standard such as a cryogenic radiometer [44–49]. Standards laboratories, attempting to make SI-traceable measurements of radiant power in the THz range, have employed varied methods including radiometric techniques known from optics [45,50], and electrically calibrated thermopile detectors with a vertically aligned carbon nanotube array (VANTA) as the absorber for the far infared (FIR) [15,46,51]. These thermal detectors are sensitive to thermal noise from the environment and are good for calibration in the milliwatt power range. To achieve greater sensitivity, into the nanowatt range, requires careful insulation of the sensor [52,53]. Comparisons of THz power measurements conducted between international standards laboratories typically yield agreement with uncertainties of a few percent [43]. Nevertheless, precise

calibration of THz sources and detectors remains challenging, and typically relies on the considerable infrastructure of national standards laboratories to provide benchmark measurements [15,39–44,46,50–55], leaving a gap in the market for a compact measurement system capable of round-robin measurements.

In recent years, Rydberg atoms have emerged as an extremely sensitive tool for radio-frequency (RF) and microwave measurement [56,57]. The so-called "Rydberg states" of alkali atoms are those with their outer electrons excited to a high principal quantum number. These states are extremely sensitive to perturbations from weak electric fields and support very strong electric dipole transitions, making them excellent detectors of weak RF fields at their transition frequencies [58,59]. Due to the relatively close spacing of transition frequencies among Rydberg states, optical detection using electromagnetically induced transparency (EIT) in thermal vapors [60] has enabled numerous demonstrations of measurement in the microwave region [61–65]. These techniques have demonstrated unprecedented sensitivity [66], high phase sensitivity [67], and vector field determination [68,69]. Real time imaging in the THz range has also been demonstrated using Rydberg atoms in a thermal vapor [70,71]. The well-known and calculable properties of such atomic systems allows for SI-traceable measurements of electric fields, negating much of the need for thermally based calibration that would typically require access to national standards laboratories [59].

In this paper, we use Rydberg atoms in a thermal vapor to demonstrate sensitive electrometry in the THz frequency range. We demonstrate our technique at a frequency of 1.06 THz, but the method is applicable across the THz and millimeter-wave range. Unlike most other THz metrology techniques, this apparatus allows for the combination of compact, cryogen-free measurements that have rapid optical readout and are robust to changing environmental conditions. Furthermore, through the well-known properties of the atomic states, the measurements can be traced to SI units.

2. METHODS

In this paper, we demonstrate THz electrometry using laser spectroscopy in an atomic vapor. The technique employs three infrared lasers to promote atoms to high-lying Rydberg states that are sensitive to applied RF fields. The experimental setup is shown in Figs. 1(a), and 1(b) shows the energy levels in ^{85}Rb to which the three infrared lasers are coupled. The probe beam (dashed green line) has a wavelength of 780 nm [external cavity diode laser (ECDL), Toptica DLpro] and is stabilized to the $5S_{1/2}(F=3) \rightarrow 5P_{3/2}(F'=4)$ transition. The dressing beam (solid blue line) has a wavelength of 1366 nm (ECDL, Toptica DLpro) and is stabilized to the $5P_{3/2}(F'=4) \rightarrow 6S_{1/2}(F''=3)$ transition. Finally, the Rydberg beam (solid red line) has a wavelength of 752 nm (MSquared, SolsTiS) and scans across the $6S_{1/2} \rightarrow 23P_{3/2}$ transition. Once the atoms have reached this highly excited Rydberg state, they can then be used to sense a THz field with a frequency of 1.06 THz (orange line) by coupling to the $23P_{3/2} \rightarrow 25S_{1/2}$ transition. The Rydberg laser is overlapped with the dressing beam using a dichroic mirror, before being directed into the cell. The probe beam counterpropagates with respect to the dressing and Rydberg beams, and is also cross polarized, meaning that it can be separated from the other two beams using a polarizing beam splitter before being detected at a photodiode. The three beams are all focused into the cuboid quartz cell (with

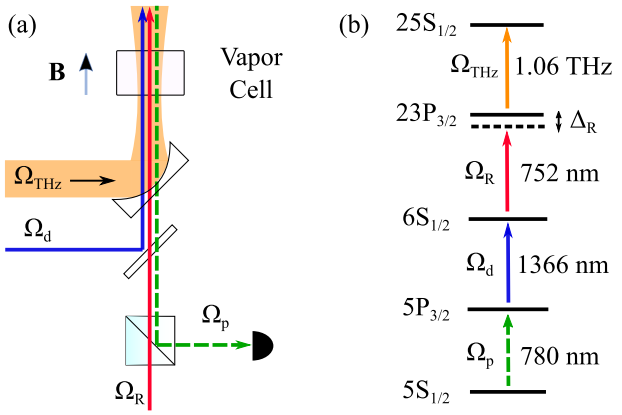

Fig. 1. (a) Experimental setup showing the geometry and propagation directions of all lasers, the THz field, and the magnetic field. All fields overlap within the 1 cm long natural abundance rubidium cell. The $1/e^2$ beam waists of the probe, dressing, and Rydberg lasers are 80 μm, 191 μm, and 85 μm, respectively, while the THz beam has a waist of 1.19 mm, focused by a parabolic mirror with a hole in the mirror to let the lasers through. These fields drive resonant transitions with Rabi frequencies Ω_p, Ω_d, Ω_R, and Ω_{THz}. (b) ^{85}Rb energy level diagram showing the transitions coupled by our light fields. Δ_R is the frequency detuning of the Rydberg laser.

window cross section 1 cm^2), which contains rubidium vapor of natural isotopic abundances. The $1/e^2$ beam waists are 80 μm, 191 μm, and 85 μm, and the powers are 1.6 nW, 21 μW, and 98 mW for the probe, dressing, and Rydberg lasers, respectively. The linewidths of all three lasers are approximately 300 kHz.

In the experiment, the vapor cell is heated to 50°C with a ceramic heater, which increases the density of the rubidium vapor to $N = 1.4 \times 10^{17}$ m^{-3}. Six homemade shim coils [not shown in Fig. 1(a)] are used to cancel the Earth's magnetic field and define a quantization axis for the atoms. The remaining field is approximately 100 mG in magnitude, with a field vector **B** parallel to the lasers' propagation directions, as noted in Fig. 1(a). This axis is important, as it can be used to selectively excite specific magnetic sub-levels within the atoms. By using the **B** field and lasers with linear polarization, we can eliminate any π transitions, leaving only σ^+ and σ^- transitions. Thus for the THz coupling between the two Rydberg levels ($23P_{3/2}$ and $25S_{1/2}$), we can average over allowed transitions to gain a more accurately defined dipole moment to use in the calculation of the THz electric field amplitude, E_{THz}.

The THz field is generated from an amplifier multiplier chain (AMC) manufactured by Virginia Diodes Inc., which is seeded with a microwave source. The THz radiation is launched into free space from a diagonal horn antenna (model WM-250/WR-1.0). In Fig. 1(a), the initial orange shaded region to the left-hand side of the figure is the THz beam after having been collimated using a parabolic mirror (not shown in the figure). Another off-axis parabolic mirror of focal length 150 mm is then used to focus the THz beam into the cell. A hole in this mirror allows the THz beam to be overlapped with the three laser beams. The $1/e^2$ beam waist of the THz beam in the cell center is estimated to be 1.2 mm, which is significantly larger than, and encompasses, the laser beams. The power of the THz beam can be adjusted through a voltage controlled attenuator (VCA) of the THz source. When very low THz powers were required (for example, in Section 3.B), THz filters made of polytetrafluoroethylene (PTFE) with fixed attenuation are

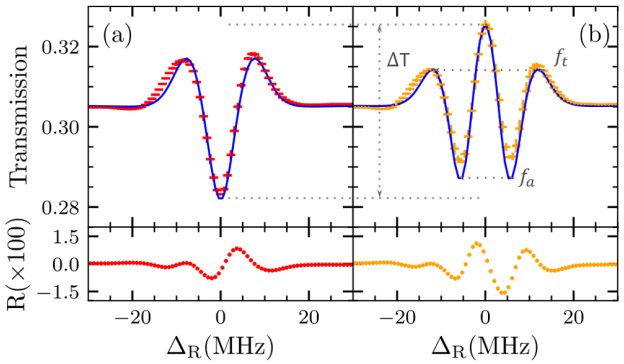

Fig. 2. EIT signal profile comparison between (a) THz off and (b) THz on, while scanning Rydberg light over detuning range Δ_R. The y axis shows the percentage probe transmission. The experimental data are an average of five repetitions, and this is where the standard error comes from. The red dots in (a) are experimental data when the THz is off, and the orange dots in (b) are experimental data when the THz is on. The blue solid lines in both (a) and (b) are theoretical modeling results using five-level Lindblad equations (see Supplement 1). The Rabi frequencies of the lasers used in the modeling are 0.5 MHz, 5.5 MHz, and 7.5 MHz for the probe, dressing, and Rydberg beams, respectively, while the THz Rabi frequency used in (b) is 11 MHz.

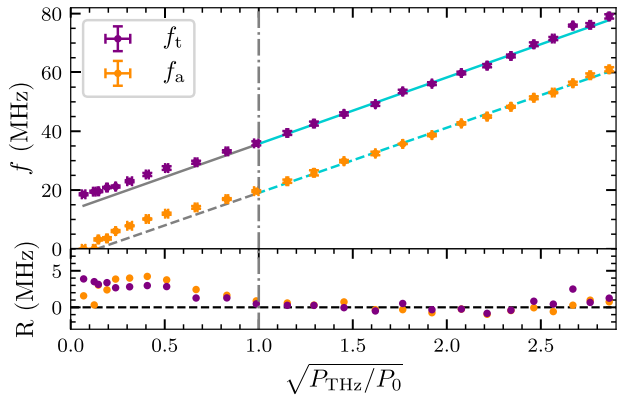

Fig. 3. Frequency splitting of the EIT signal features: f_a and f_t versus $\sqrt{P_{\mathrm{THz}}/P_0}$, where P_{THz} is THz power measured at the output of the source by a THz calorimeter (PM5). The data are divided into low and high power THz regimes by a vertical gray line at $\sqrt{P_{\mathrm{THz}}/P_0} = 1$, where $P_0 = 11.6\ \mu$W. The purple and yellow dots are experimental data points for f_t and f_a, respectively. The cyan solid and dashed lines are straight line fits to the corresponding datasets in the high power THz regime. These fits are projected into the low power regime for illustrative purposes. The lower panel shows the residuals for both datasets, which demonstrate a high degree of agreement in the high power regime.

used in the THz beam path to reduce the THz power reaching the cell.

The probe and dressing lasers are stabilized to their respective transitions using polarization spectra [72]. By scanning the detuning of the Rydberg laser (Δ_R), a three-photon EIT signal [73] is observed by measuring the probe transmission using the photodiode. A typical EIT spectrum is shown in Fig. 2(a). The EIT signal has an absorptive dip on resonance and off-resonant transmission peaks either side of resonance. These peaks are separated by a frequency f_t, which depends upon the intensity, and therefore Rabi frequency (Ω_d), of the dressing laser. When the THz field is applied, the EIT spectrum changes [see Fig. 2(b)], and as the THz field strength is increased, the central absorption feature begins to split and on-resonant transmission increases. This Autler–Townes (AT) splitting of the absorption feature is parameterized as f_a. The data shown in Fig. 2 are an average of five repetitions taken in a total integration time of 3 ms with a scanning rate of 100 MHz/ms. The solid blue lines in Fig. 2 are the results of numerically solving the Lindblad equations (see Supplement 1). The experimental results agree well with the theoretical modeling, as shown by the residuals in the lower panels.

3. RESULTS

The EIT traces in Fig. 2 are typical of the spectra used to extract the THz field intensity information. Specifically, the AT splitting of the absorptive spectral feature f_a, the splitting of the transmission features f_t, and the resonant transmission change ΔT are analyzed at different THz intensities.

For the purposes of our analysis, we demarcate two regimes of incident THz power: the low power regime, and the high power regime. In the low power regime, when f_a is smaller than twice the linewidth of the bare EIT feature, the relationship between splitting and incident THz power is nonlinear [74]. Thus, we use the resonant transmission change ΔT to indicate the THz amplitude. However, in the high power regime, the relationship between AT splitting and applied THz field amplitude, E_{THz}, is linear and related through [65]

$$2\pi\hbar f_a = \hbar\Omega_{\mathrm{THz}} = \mu E_{\mathrm{THz}}, \tag{1}$$

where μ is the dipole moment of the THz transition, $\hbar$ is the reduced Planck's constant, and Ω_{THz} is the THz Rabi frequency. Therefore, we can directly relate the measured splitting to the THz electric field if we know the value of the atomic dipole moment, μ.

Figure 3 shows the evolution of f_t (purple dots) and f_a (yellow dots) with the square root of the incident THz power $\sqrt{P_{\mathrm{THz}}}$. Note that the measurements of P_{THz} on the x axis in Fig. 3 are derived from direct measurements at the source using a waveguide-coupled commercial calorimetric THz power meter (VDI Erickson, PM5). Due to the losses of THz power in our beam path, such as reflection from the glass cell walls, the true THz power reaching the atoms in the vapor cell is expected to be significantly lower than measured at the source, reduced by a systematic attenuation factor. For clarity, since the absolute power cannot be measured inside the cell, we scale the power relative to P_0, where $P_0 = 11.6\ \mu$W, corresponding to an AT splitting f_a equal to twice the linewidth of the bare EIT feature.

The data in Fig. 3 are partitioned into the low and high power THz regimes following the definition above by a gray vertical line at $P_{\mathrm{THz}} = P_0$. On the right-hand side, the THz-induced splitting is twice as large as the THz-free EIT signal linewidth; therefore, AT splitting is dominant and proportional to $\sqrt{P_{\mathrm{THz}}}$ [75]. On the left-hand side, the relationship between f_a and $\sqrt{P_{\mathrm{THz}}}$ is not linear, and we discuss the calibration of this power range in Section 3.B.

A. High THz Power Regime

In Fig. 3, on the right-hand side, the cyan solid and dashed lines are least-squares straight line fits to the corresponding datasets in the high power THz regime. These fits are also projected into the low power regime for illustrative purposes to show the deviation from linearity in this region. The lower panel shows the residuals for both datasets, which demonstrate good linearity in the high power region.

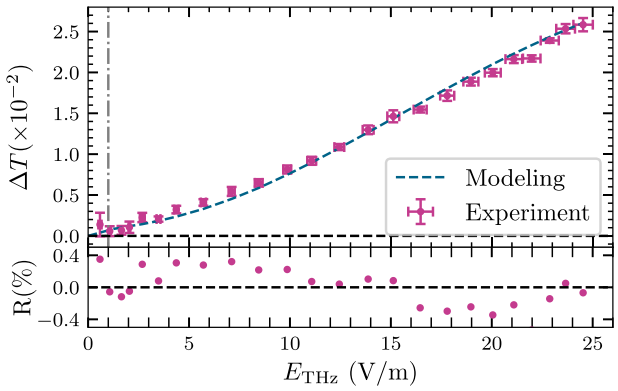

Fig. 4. Probe transmission difference between THz on and THz off (ΔT) versus THz electrical field amplitude E_{THz}. The pink dots are experimental data points, and the dashed blue curve is the theory modeling results from the Lindblad equations (see Supplement 1). The dashed gray line indicates the data points where the lower errorbars hit zero, indicating the minimum detectable power. The lower panel is the residual plot.

In the linear region, the data for f_t and f_a show fitted gradients that match within the uncertainty of measurement, while f_t has an initial frequency width when the THz power is zero, as shown in Fig. 2(a). The residual plot in Fig. 3 reveals a small deviation from linearity that may be caused by off-resonant state couplings [76]. The AT splitting f_a can be used to calculate the THz electric field directly using Eq. (1) with the dipole moment of the THz transition $\mu_{\mathrm{THz}} = 31.17\ ea_0$ [77]. This relation is also used to calculate the electric field on the x axis in Fig. 4 used for the low power regime calibration.

B. Low THz Power Regime

When $\sqrt{P_{\mathrm{THz}}/P_0} < 1$ in Fig. 3, the relationship between the splittings and $\sqrt{P_{\mathrm{THz}}}$ is not linear [65,75], and it is no longer possible to extract an electric field value from the splitting. The deviation from the linear fitting for this low power region is well illustrated in the residual plot in Fig. 3. This nonlinearity is due to a quantum interference effect when the THz Rabi frequency is comparable to the Rabi frequencies of the IR lasers [75,78]. In this regime, we can instead use the resonant transmission change ΔT [shown in Fig. 2(b)] as a probe of E_{THz}. The relationship between ΔT and electric field amplitude E_{THz} of THz is shown in Fig. 4. Here the very low THz amplitude is achieved by attenuating the THz beam using PTFE blocks with a total thickness of 5.7 cm.

We first calibrated the PTFE attenuators from the linear trend of the AT splitting (see Supplement 1). Then the attenuators were combined, resulting in a transmitted THz power of $T_a = (2.22 \pm 0.08)\%$ into the cell. Thus, the incident THz field E_{THz} in the x axis in Fig. 4 is able to be calibrated from Eq. (1) and T_a.

In Fig. 4, the pink dots are experimental data of resonant transmission of THz on minus THz off (ΔT) from five repetitions. The uncertainty in E_{THz} is due to uncertainty in the calibration of the atomic sensor from the linear trend. The dashed blue line is the theory modeling results generated using the Lindblad equations (see Supplement 1). There is a high level of agreement between our predictions and the experimental data.

The minimum detectable THz field amplitude point is chosen where the errorbars of ΔT data intersect with zero splitting, indicated by the gray line in Fig. 4. The figure shows that this occurs at approximately (1.07 ± 0.06) V/m corresponding to a THz power of (5.6 ± 0.3) nW output from the THz source. At this point the THz-on signal can no longer be reliably distinguished from the THz-off signal within the noise of the measurement.

4. DISCUSSION

In the experiment, the largest source of THz power loss during its propagation is due to reflection and absorption by the fused quartz cell (JGS1). The refractive index of fused quartz for a 1.06 THz field is approximately 1.953, and the absorption coefficient is approximately 2.3 cm^{-1} [79]. Thus, 10% of the power is reflected from each quartz surface. For our cell, with a wall thickness of 1.25 mm, the absorption of the THz by one cell wall is 25%. Therefore, a total 40% of the THz power is lost before it reaches the atoms. Further to this, the surfaces of the gold parabolic mirrors are not perfectly reflective, though generally they have a reflectivity of over 99% at 1.06 THz. [79]. Finally, the property of THz radiation being strongly absorbed by water may have contributed to a reduction in amplitude due to the relative humidity of the laboratory. We estimate therefore that approximately 40% of the THz power is lost in the propagation path before reaching the atoms in the vapor cell. When accounting for this, the minimum detectable power of THz radiation on the atomic cell is approximately 3.4 nW for a total integration time of 3 ms. For comparison, this value is 0.3% of the lower detection limit of 1 μW from the calorimeter power meter (PM5) requiring an integration time of 45 s.

Despite this performance, there is still scope for improvements. First, a narrower linewidth Rydberg laser [80,81] will minimize frequency drifts, which bring the uncertainty to both frequency splitting and transmission measurements. Second, the use of a lock-in amplifier could reduce the minimum detectable intensity by reducing the noise floor of the measurements [65,74]. Third, the application of a well-designed THz waveguide attached to the cell together with an antireflection coating on the cell surface could potentially avoid the losses in the THz propagation to the atoms and make the system more compact. Finally, the scanning rate of the laser could be increased to reduce the acquisition time.

The theoretical modeling of the system presented in Supplement 1, and shown in Fig. 2, illustrates that we can reproduce the observed behavior of the experimental system. It provides confidence that Eq. (1) can be applied directly in the high power regime to extract a value for the THz electric field from the splitting observed in the spectra; the full modeling does not need to be reproduced to extract a field measurement, greatly simplifying the analysis.

Although our demonstration is at a frequency of 1.06 THz, we could choose any frequency at which there is an available atomic transition. Furthermore, the choice of frequency can be further expanded by using another alkali metal vapor, such as cesium or potassium. Figure S2 in Supplement 1 shows all accessible frequencies in the range of 0.3–3.0 THz for rubidium, cesium, and potassium. The transition we use here is highlighted by the black dot. This transition has an average sized dipole moment, so for other frequencies, the sensitivity could be greater or smaller.

It is not possible to make a direct comparison of the sensitivity of this three-photon system to the more typical two-photon EIT system [69] employed in Rydberg microwave detection. This is partly because the schemes access different atomic energy levels. The coupling strength for the THz transition will be different depending on the path chosen in each case, and therefore the

THz responsivity will also differ. Also, the laser wavelengths used in three-photon and two-photon systems are very different, so the Doppler cancellation effects on the EIT linewidth are also different. It is possible to choose transitions in a three-photon system with laser wavelengths that can completely eliminate Doppler broadening [82], which is more difficult to achieve in a two-photon system. Finally, the EIT linewidth and signal to noise ratio depend on the laser powers for both systems. The lower the power used, the smaller the broadening of the linewidth, and the smaller the shot noise. However, a lower power would mean that the signal to noise ratio is worse. It is a trade-off choice for both systems. We note that for the commercialization of these Rydberg RF sensor systems, our all-IR method may provide an advantage, as it avoids the requirement of an expensive, high power visible laser system, typically achieved via frequency doubling.

5. CONCLUSION

In this paper, we have demonstrated an SI-traceable THz detection system using three IR lasers to excite room temperature atoms to a Rydberg state that is sensitive to THz radiation.

We have shown that it is possible to calibrate stronger THz electric field amplitudes to SI units using the frequency splitting caused by the AT effect. For weaker THz fields, it is still possible to calibrate our sensor by using the resonant transmission change induced in the EIT signal, which is traceable to SI units with the help of THz attenuators that can be first characterized using the AT range of our system. The minimum detectable power achieved here is (1.07 ± 0.06) V/m at 1.06 THz (3 ms of total integration time), corresponding to a THz power of approximately 3.4 nW inside the cell. Because of the relative simplicity and low cost nature of the room temperature working device, it has the potential to provide a route to a SI traceable "atomic candle" for THz calibration in industrial settings.

Funding. Horizon 2020 Framework Programme (820393); Engineering and Physical Sciences Research Council (M014398/1, R002061/1, S015973/1).

Acknowledgment. The authors thank Zhongxiao Xu and Chris Wade for useful discussions.

Disclosures. The authors declare no conflicts of interest.

Data availability. Data underlying the results presented in this paper are available at [83].

Supplemental document. See Supplement 1 for supporting content.

REFERENCES

1. S. S. Dhillon, M. S. Vitiello, E. H. Linfield, *et al.*, "The 2017 terahertz science and technology roadmap," J. Phys. D. **50**, 043001 (2019).
2. A. Y. Pawar, D. D. Sonawane, K. B. Erande, and D. V. Derle, "Terahertz technology and its applications," Drug Invent. Today **5**(2), 157–163 (2013).
3. M. Naftaly, N. Vieweg, and A. Deninger, "Industrial applications of terahertz sensing: state of play," Sensors **19**, 4203 (2019).
4. R. M. Woodward, V. P. Wallace, R. J. Pye, B. E. Cole, D. D. Arnone, E. H. Linfield, and M. Pepper, "Terahertz pulse imaging of ex vivo basal cell carcinoma," J. Invest. Dermatol. **120**, 72–78 (2003).
5. L. Yu, L. Hao, T. Meiqiong, H. Jiaoqi, L. Wei, D. Jinying, C. Xueping, F. Weiling, and Z. Yang, "The medical application of terahertz technology in non-invasive detection of cells and tissues: opportunities and challenges," RSC Adv. **9**, 9354–9363 (2019).
6. M. C. Kemp, P. Taday, B. E. Cole, J. Cluff, A. J. Fitzgerald, and W. R. Tribe, "Security applications of terahertz technology," Proc. SPIE **5070**, 44–52 (2003).
7. J. Federici and L. Moeller, "Review of terahertz and subterahertz wireless communications," J. Appl. Phys. **107**, 111101 (2010).
8. M. Tonouchi, "Cutting-edge terahertz technology," Nat. Photonics **1**, 97–105 (2007).
9. R. Müller, W. Bohmeyer, M. Kehrt, K. Lange, C. Monte, and A. Steiger, "Novel detectors for traceable THz power measurements," J. Infrared Millim. Terahertz Waves **35**, 659–670 (2014).
10. R. Lewis, "A review of terahertz detectors," J. Phys. D **52**, 433001 (2019).
11. S. Seliverstov, S. Maslennikov, S. Ryabchun, M. Finkel, T. Klapwijk, N. Kaurova, Y. Vachtomin, K. Smirnov, B. Voronov, and G. Goltsman, "Fast and sensitive terahertz direct detector based on superconducting antenna-coupled hot electron bolometer," IEEE Trans. Appl. Supercond. **25**, 1–4 (2014).
12. X. Zhao, Y. Wang, J. Schalch, G. Duan, K. Cremin, J. Zhang, C. Chen, R. D. Averitt, and X. Zhang, "Optically modulated ultra-broadband all-silicon metamaterial terahertz absorbers," ACS Photon. **6**, 830–837 (2019).
13. A. Shurakov, Y. Lobanov, and G. Goltsman, "Superconducting hot-electron bolometer: from the discovery of hot-electron phenomena to practical applications," Supercond. Sci. Technol. **29**, 023001 (2015).
14. C. Wu, W. Zhou, N. Yao, X. Xu, Y. Qu, Z. Zhang, J. Wu, L. Jiang, Z. Huang, and J. Chu, "Silicon-based high sensitivity of room-temperature microwave and sub-terahertz detector," Appl. Phys. Express **12**, 052013 (2019).
15. J. H. Lehman, B. Lee, and E. N. Grossman, "Far infrared thermal detectors for laser radiometry using a carbon nanotube array," Appl. Opt. **50**, 4099–4104 (2011).
16. D. R. Denison, M. E. Knotts, M. E. McConney, and V. V. Tsukruk, "Experimental characterization of mm-wave detection by a micro-array of Golay cells," Proc. SPIE **7309**, 73090J (2009).
17. A. Rogalski and F. Sizov, "Terahertz detectors and focal plane arrays," Opto-electron. Rev. **19**, 346–404 (2011).
18. R. Müller, B. Gutschwager, J. Hollandt, M. Kehrt, C. Monte, R. Müller, and A. Steiger, "Characterization of a large-area pyroelectric detector from 300 GHz to 30 THz," J. Infrared Millim. Terahertz Waves **36**, 654–661 (2015).
19. W. Li, Z. Liang, J. Wang, J. Gou, and Y. Jiang, "A direct method of thermal time constant measurement for lithium tantalate based terahertz pryroelectric detectors," J. Mater. Sci. Mater. Electron. **27**, 9996–10002 (2016).
20. J. A. Russer, C. Jirauschek, G. P. Szakmany, M. Schmidt, A. O. Orlov, G. H. Bernstein, W. Porod, P. Lugli, and P. Russer, "High-speed antenna-coupled terahertz thermocouple detectors and mixers," IEEE Trans. Microw. Theory Tech. **63**, 4236–4246 (2015).
21. S. Kono, M. Tani, P. Gu, and K. Sakai, "Detection of up to 20 THz with a low-temperature-grown GaAs photoconductive antenna gated with 15 fs light pulses," Appl. Phys. Lett. **77**, 4104–4106 (2000).
22. M. Sakhno, A. Golenkov, and F. Sizov, "Uncooled detector challenges: millimeter-wave and terahertz long channel field effect transistor and Schottky barrier diode detectors," J. Appl. Phys. **114**, 164503 (2013).
23. S. A. Maas, *Nonlinear Microwave and RF Circuits* (Artech House, 2003).
24. S. Preu, M. Mittendorff, S. Winnerl, O. Cojocari, and A. Penirschke, "THz autocorrelators for ps pulse characterization based on Schottky diodes and rectifying field-effect transistors," IEEE Trans. Terahertz Sci. Technol. **5**, 922–929 (2015).
25. S.-P. Han, H. Ko, J.-W. Park, N. Kim, Y.-J. Yoon, J.-H. Shin, D. Y. Kim, D. H. Lee, and K. H. Park, "InGaAs Schottky barrier diode array detector for a real-time compact terahertz line scanner," Opt. Express **21**, 25874–25882 (2013).
26. X. He, N. Fujimura, J. M. Lloyd, K. J. Erickson, A. A. Talin, Q. Zhang, W. Gao, Q. Jiang, Y. Kawano, R. H. Hauge, F. Léonard, and J. Kono, "Carbon nanotube terahertz detector," Nano Lett. **14**, 3953–3958 (2014).
27. M. S. Vitiello, D. Coquillat, L. Viti, D. Ercolani, F. Teppe, A. Pitanti, F. Beltram, L. Sorba, W. Knap, and A. Tredicucci, "Room-temperature terahertz detectors based on semiconductor nanowire field-effect transistors," Nano Lett. **12**, 96–101 (2012).
28. H. Qin, J. Sun, Z. He, X. Li, X. Li, S. Liang, C. Yu, Z. Feng, X. Tu, B. Jin, J. Chen, and P. Wu, "Heterodyne detection at 216, 432, and 648 GHz based on bilayer graphene field-effect transistor with quasi-optical coupling," Carbon **121**, 235–241 (2017).
29. T. Watanabe, S. A. Boubanga-Tombet, Y. Tanimoto, D. Fateev, V. Popov, D. Coquillat, W. Knap, Y. M. Meziani, Y. Wang, H. Minamide, H. Ito, and

T. Otsuji, "InP-and GaAs-based plasmonic high-electron-mobility transistors for room-temperature ultrahigh-sensitive terahertz sensing and imaging," IEEE Sens. J. **13**, 89–99 (2012).
30. X. Chen, H. Liu, Q. Li, H. Chen, R. Peng, S. Chu, and B. Cheng, "Terahertz detectors arrays based on orderly aligned InN nanowires," Sci. Rep. **5**, 13199 (2015).
31. Y. Kurita, G. Ducournau, D. Coquillat, A. Satou, K. Kobayashi, S. B. Tombet, Y. M. Meziani, V. V. Popov, W. Knap, T. Suemitsu, and T. Otsuji, "Ultrahigh sensitive sub-terahertz detection by InP-based asymmetric dual-grating-gate high-electron-mobility transistors and their broadband characteristics," Appl. Phys. Lett. **104**, 251114 (2014).
32. D. Coquillat, J. Marczewski, P. Kopyt, N. Dyakonova, B. Giffard, and W. Knap, "Improvement of terahertz field effect transistor detectors by substrate thinning and radiation losses reduction," Opt. Express **24**, 272–281 (2016).
33. I. S. Gregory, W. Tribe, C. Baker, B. Cole, M. Evans, L. Spencer, M. Pepper, and M. Missous, "Continuous-wave terahertz system with a 60 dB dynamic range," Appl. Phys. Lett. **86**, 204104 (2005).
34. N. Wang, S. Cakmakyapan, Y.-J. Lin, H. Javadi, and M. Jarrahi, "Room-temperature heterodyne terahertz detection with quantum-level sensitivity," Nat. Astron. **3**, 977–982 (2019).
35. T. Taimre, M. Nikolić, K. Bertling, Y. L. Lim, T. Bosch, and A. D. Rakić, "Laser feedback interferometry: a tutorial on the self-mixing effect for coherent sensing," Adv. Opt. Photon. **7**, 570–631 (2015).
36. K. Liu, J. Xu, and X.-C. Zhang, "GaSe crystals for broadband terahertz wave detection," Appl. Phys. Lett. **85**, 863–865 (2004).
37. X. Pan, Y. Cai, X. Zeng, S. Zheng, J. Li, and S. Xu, "A terahertz EO detector with large dynamical range, high modulation depth and signal-noise ratio," Opt. Commun. **391**, 135–140 (2017).
38. A. Shugurov, S. Bodrov, E. Mashkovich, H. Kitahara, N. Abramovsky, M. Tani, and M. Bakunov, "Noncollinear electro-optic sampling detection of terahertz pulses in a $LiNbO_3$ crystal while avoiding the effect of intrinsic birefringence," Opt. Express **30**, 3741–3748 (2022).
39. B. Gutschwager, C. Monte, H. Delsim-Hashemi, O. Grimm, and J. Hollandt, "Calculable blackbody radiation as a source for the determination of the spectral responsivity of THz detectors," Metrologia **46**, S165–S169 (2009).
40. J. Kendall and C. M. Berdahl, "Two blackbody radiometers of high accuracy," Appl. Opt. **9**, 1082–1091 (1970).
41. T. Kleine-Ostmann, "THz metrology," in *38th International Conference on Infrared, Millimeter, and Terahertz Waves (IRMMW-THz)* (IEEE, 2013), pp. 1–4.
42. A. Svetlitza, M. Slavenko, T. Blank, I. Brouk, S. Stolyarova, and Y. Nemirovsky, "Thz measurements and calibration based on a blackbody source," IEEE Trans. Terahertz Sci. Technol. **4**, 347–359 (2014).
43. A. Steiger, R. Müller, A. R. Oliva, Y. Deng, Q. Sun, M. White, and J. Lehman, "Terahertz laser power measurement comparison," IEEE Trans. Terahertz Sci. Technol. **6**, 664–669 (2016).
44. L. Werner, H.-W. Hübers, P. Meindl, R. Müller, H. Richter, and A. Steiger, "Towards traceable radiometry in the terahertz region," Metrologia **46**, S160–S164 (2009).
45. A. Steiger, B. Gutschwager, M. Kehrt, C. Monte, R. Müller, and J. Hollandt, "Optical methods for power measurement of terahertz radiation," Opt. Express **18**, 21804–21814 (2010).
46. M. G. White, M. L. Dowell, and J. H. Lehman, "Traceable terahertz power metrology at NIST," in *39th International Conference on Infrared, Millimeter, and Terahertz Waves (IRMMW-THz)* (IEEE, 2014), p. 1.
47. B. Globisch, R. J. Dietz, T. Göbel, M. Schell, W. Bohmeyer, R. Müller, and A. Steiger, "Absolute terahertz power measurement of a time-domain spectroscopy system," Opt. Lett. **40**, 3544–3547 (2015).
48. R. Dickhoff, C. Jastrow, A. Steiger, R. Müller, T. Kleine-Ostmann, and T. Schrader, "Characterization of THz beams," in *CLEO: Science and Innovations* (Optical Society of America, 2011), paper JThB116.
49. R. Müller, W. Bohmeyer, K. Lange, and A. Steiger, "THz metrological traceability and suitable detectors," in *CLEO: Science and Innovations* (Optical Society of America, 2012), paper CTu3B-8.
50. A. Steiger, M. Kehrt, C. Monte, and R. Müller, "Traceable terahertz power measurement from 1 THz to 5 THz," Opt. Express **21**, 14466–14473 (2013).
51. J. Lehman, M. Dowell, N. B. Popovic, K. Betz, and E. Grossman, "Laser power-meter comparison at far-infrared wavelengths and terahertz frequencies," Metrologia **49**, 583–587 (2012).
52. H. Iida, M. Kinoshita, K. Amemiya, and Y. Shimada, "Calorimetric measurement of absolute terahertz power at the sub-microwatt level," Opt. Lett. **39**, 1609–1612 (2014).
53. H. Iida, M. Kinoshita, and K. Amemiya, "Accurate measurement of absolute terahertz power using broadband calorimeter," J. Infrared Millim. Terahertz Waves **39**, 409–421 (2018).
54. Z. Popovic and E. N. Grossman, "THz metrology and instrumentation," IEEE Trans. Terahertz Sci. Technol. **1**, 133–144 (2011).
55. Y. Deng, Q. Sun, J. Yu, Y. Lin, and J. Wang, "Broadband high-absorbance coating for terahertz radiometry," Opt. Express **21**, 5737–5742 (2013).
56. C. S. Adams, J. D. Pritchard, and J. P. Shaffer, "Rydberg atom quantum technologies," J. Phys. B **53**, 012002 (2019).
57. M. Saffman, T. G. Walker, and K. Mølmer, "Quantum information with Rydberg atoms," Rev. Mod. Phys. **82**, 2313–2363 (2010).
58. M. Tanasittikosol, J. D. Pritchard, D. Maxwell, A. Gauguet, K. J. Weatherill, R. M. Potvliege, and C. S. Adams, "Microwave dressing of Rydberg dark states," J. Phys. B **44**, 184020 (2011).
59. J. A. Sedlacek, A. Schwettmann, H. Kübler, R. Löw, T. Pfau, and J. P. Shaffer, "Microwave electrometry with Rydberg atoms in a vapour cell using bright atomic resonances," Nat. Phys. **8**, 819–824 (2012).
60. A. Mohapatra, T. Jackson, and C. Adams, "Coherent optical detection of highly excited Rydberg states using electromagnetically induced transparency," Phys. Rev. Lett. **98**, 113003 (2007).
61. C. L. Holloway, J. A. Gordon, A. Schwarzkopf, D. A. Anderson, S. A. Miller, N. Thaicharoen, and G. Raithel, "Sub-wavelength imaging and field mapping via electromagnetically induced transparency and Autler-Townes splitting in Rydberg atoms," Appl. Phys. Lett. **104**, 244102 (2014).
62. H. Fan, S. Kumar, H. Kübler, and J. Shaffer, "Dispersive radio frequency electrometry using Rydberg atoms in a prism-shaped atomic vapor cell," J. Phys. B **49**, 104004 (2016).
63. S. Li, J. Yuan, and L. Wang, "Improvement of microwave electric field measurement sensitivity via multi-carrier modulation in Rydberg atoms," Appl. Sci. **10**, 8110 (2020).
64. H. Fan, S. Kumar, J. Sedlacek, H. Kübler, S. Karimkashi, and J. P. Shaffer, "Atom based RF electric field sensing," J. Phys. B **48**, 202001 (2015).
65. C. L. Holloway, J. A. Gordon, S. Jefferts, A. Schwarzkopf, D. A. Anderson, S. A. Miller, N. Thaicharoen, and G. Raithel, "Broadband Rydberg atom-based electric-field probe for SI-traceable, self-calibrated measurements," IEEE Trans. Antennas Propag. **62**, 6169–6182 (2014).
66. M. Jing, Y. Hu, J. Ma, H. Zhang, L. Zhang, L. Xiao, and S. Jia, "Atomic superheterodyne receiver based on microwave-dressed Rydberg spectroscopy," Nat. Phys. **16**, 911–915 (2020).
67. D. A. Anderson, R. E. Sapiro, and G. Raithel, "Rydberg atoms for radio-frequency communications and sensing: atomic receivers for pulsed RF field and phase detection," IEEE Aerosp. Electron. Syst. Mag. **35**(4), 48–56 (2020).
68. A. K. Robinson, N. Prajapati, D. Senic, M. T. Simons, and C. L. Holloway, "Determining the angle-of-arrival of a radio-frequency source with a Rydberg atom-based sensor," Appl. Phys. Lett. **118**, 114001 (2021).
69. J. Sedlacek, A. Schwettmann, H. Kübler, and J. Shaffer, "Atom-based vector microwave electrometry using rubidium Rydberg atoms in a vapor cell," Phys. Rev. Lett. **111**, 063001 (2013).
70. C. G. Wade, N. Šibalić, N. R. de Melo, J. M. Kondo, C. S. Adams, and K. J. Weatherill, "Real-time near-field terahertz imaging with atomic optical fluorescence," Nat. Photonics **11**, 40–43 (2017).
71. L. A. Downes, A. R. MacKellar, D. J. Whiting, C. Bourgenot, C. S. Adams, and K. J. Weatherill, "Full-field terahertz imaging at kilohertz frame rates using atomic vapor," Phys. Rev. X **10**, 011027 (2020).
72. C. Carr, C. S. Adams, and K. J. Weatherill, "Polarization spectroscopy of an excited state transition," Opt. Lett. **37**, 118–120 (2012).
73. C. Carr, M. Tanasittikosol, A. Sargsyan, D. Sarkisyan, C. S. Adams, and K. J. Weatherill, "Three-photon electromagnetically induced transparency using Rydberg states," Opt. Lett. **37**, 3858–3860 (2012).
74. C. L. Holloway, M. T. Simons, J. A. Gordon, A. Dienstfrey, D. A. Anderson, and G. Raithel, "Electric field metrology for SI traceability: systematic measurement uncertainties in electromagnetically induced transparency in atomic vapor," J. Appl. Phys. **121**, 233106 (2017).
75. L. Hao, Y. Xue, J. Fan, Y. Jiao, J. Zhao, and S. Jia, "Nonlinearity of microwave electric field coupled Rydberg electromagnetically induced transparency and Autler-Townes splitting," Appl. Sci. **9**, 1720 (2019).

76. A. Chopinaud and J. D. Pritchard, "Optimal state choice for Rydberg-atom microwave sensors," Phys. Rev. Appl. **16**, 024008 (2021).
77. N. Šibalić, J. D. Pritchard, C. S. Adams, and K. J. Weatherill, "ARC: an open-source library for calculating properties of alkali Rydberg atoms," Comput. Phys. Commun. **220**, 319–331 (2017).
78. L. Hao, Y. Jiao, Y. Xue, X. Han, S. Bai, J. Zhao, and G. Raithel, "Transition from electromagnetically induced transparency to Autler–Townes splitting in cold cesium atoms," New J. Phys. **20**, 073024 (2018).
79. Y.-S. Lee, *Principles of Terahertz Science and Technology* (Springer, 2009), Vol. **170**.
80. D. J. Reed, N. Šibalić, D. J. Whiting, J. M. Kondo, C. S. Adams, and K. J. Weatherill, "Low-drift Zeeman shifted atomic frequency reference," OSA Contin. **1**, 4–12 (2018).
81. E. D. Black, "An introduction to Pound–Drever–Hall laser frequency stabilization," Am. J. Phys. **69**, 79–87 (2001).
82. J. P. Shaffer, "Atom-based electromagnetic field sensing (Conference Presentation)," Proc. SPIE **11296**, 112960Q (2020).
83. S. Chen, "Terahertz electrometry via infrared spectroscopy of atomic vapor," Durham University, 30 March 2022, https://doi.org/10.15128/r24f16c287m.